Modeling of Near-Field Effects in Sub-Wavelength Deep Ultraviolet Lithography

J. Tirapu Azpiroz and E. Yablonovitch
Electrical Engineering Dept., UCLA, Los Angeles, CA 90095-1594, U.S.A.

1. Introduction

To maintain the historical trend of doubling chip density roughly every eighteen months while maintaining a nearly constant chip price, the semiconductor industry now performs lithography within the *subwavelength* regime in deep ultraviolet (DUV) lithography. Several resolution enhancement techniques (RET) have been developed and increasingly employed, together with imaging systems of higher numerical aperture (*NA*), to enable this steady reduction of wafer critical dimensions (CD) below the illumination wavelength.

These conditions place a serious limitation on conventional scalar simulations of the lithographic image based on Kirchhoff boundary conditions to approximate the field immediately behind the patterned mask. This approximation fails to account for the increasingly important topographical effects of the mask[1-3] (thick mask effects). Our chapter presents a boundary layer (BL) model to overcome this problem. In addition, our approach accounts for the oblique directions of propagation of light through optical systems with high numerical aperture.[4-6]

Aerial images at the wafer plane produced by rigorous electromagnetic (EM) solutions of the field on the mask were evaluated by means of a vectorial formulation of the imaging process. This was then compared to ideal images produced by the thin mask approximation, where the field on the mask openings was replaced by the incident field. Our new model consists of a sophisticated version of the Kirchhoff approximation, capable of modeling thick mask effects by simply adding a fixed-width, locally-determined boundary layer to every edge. Polarization and edge diffraction effects, as well as phase and transmission errors, are included in our model by permitting a complex transmission coefficient in the boundary layer.

2. Boundary layer model

Boundary layers are already employed in industry to account for the losses in peak intensity of the field traveling through small apertures in the chrome mask, but always in the form of a bias, that is, an opaque boundary layer. However, some of these topographic effects (polarization dependence of the boundary conditions, phase and amplitude transmission errors) arising from the vector nature of light become particularly critical for alternating phase-shifting (PSM) masks,[7] which

demand rigorous resource-consuming 3D EM field simulations in the subwavelength regime.

Several modeling methods have therefore been studied in literature.[8-10] Lam and Neureuther's recent "domain decomposition method"[10] employs pre-calculated diffracted fields from isolated edges that are added afterwards according to the diffracting patterns. Based on the linearity of Maxwell's equations, this method provides exact results for infinitely long edges and reasonably good accuracy for complex patterns. There is a heavy computational burden of superposing many edges to make an image and the resulting superposition is non-rigorous.

Yan's approach[9] shares with our boundary layer model the possibility of locally modeling topographical mask effects with a boundary band of different transmission coefficient at the thin mask edges. Yan's model approximates the diffraction effects on the edges of extreme ultraviolet (EUV) lithography of infinite lines of width 2.23λ, by adding a strip to the thin mask model. However, in his approach, the width and transmission coefficients of the boundary layer were obtained by matching the diffraction ripples of the near field evaluated on the mask surface. For the complex DUV transmission masks analyzed in this paper, we performed a systematic study of rectangles of different aspect ratios and sizes, and selected the boundary layer parameters to optimize the central field amplitude on the wafer, not the mask.

Alternating PSM masks have etching profiles with abrupt discontinuities, as sketched in Fig. 1 for clear and 180° phase-shift openings with and without 35 nm undercut. Rigorously evaluated fields on thick chrome mask apertures exhibit effects such as those observed in Fig. 2(a) of the electric field immediately below a square 180° phase-shift opening of 3λ side length (λ = 248 nm) and horizontally polarized incident electric field, evaluated by a finite difference time domain (FDTD) algorithm Tempest 5.0.[2] Direct application of Kirchhoff's boundary conditions[11] provides a thin mask approximation of the object field on the exit surface of the mask, obtained by multiplying the incident field times an ideal transmission function with the mask pattern as plotted in Fig. 2(b). This model ignores the standing wave patterns and other polarization effects observed in Fig. 2(a) and turns out to be very inaccurate for feature sizes of the order of λ. Our model, which retains much of the thin mask simplicity, is displayed in Fig. 2(c), where an imaginary boundary layer is applied to the same 3λ 180° phase-shift square opening and horizontally polarized incident light.

Notice the directional dependence of the boundary layer transmission coefficient that reaches its maximum value when the electric field is tangent to the

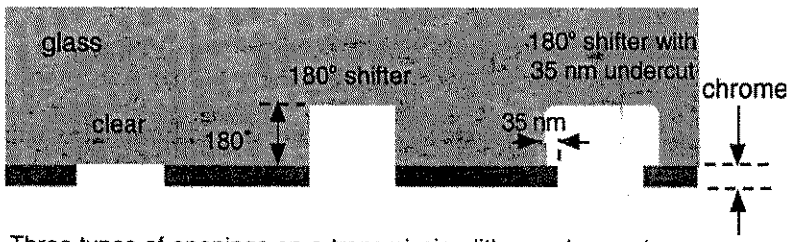

Figure 1. Three types of openings on a transmission lithography mask.

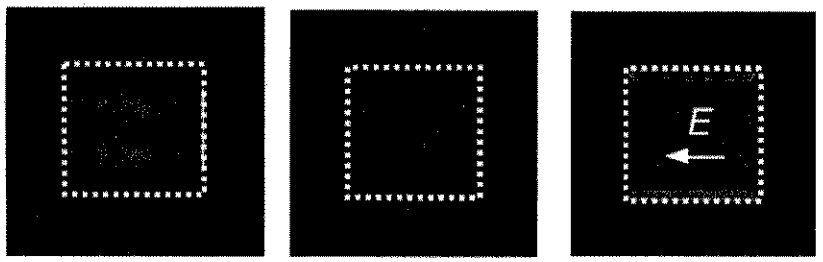

Figure 2. (a) Sketch of the actual field calculated by FDTD on the aperture of a 3λ 180°-shifter square opening with horizontally polarized electric field. (b) Kirchhoff scalar approximation (thin mask model) of the field on the same aperture. (c) Boundary layer model for the same square opening and illumination.

boundary and diminishes to zero when the field is normal to it. This simple geometric rule (cosine rule) accounts for the orientation dependence of the boundary conditions at the metal edges. Tangential components of the electric field must vanish on metal surfaces, setting up conditions for standing-wave effects on the aperture field that contribute to the phase errors. Normal electric field components, on the other hand, exhibit a discontinuity due to the accumulation of charges on the chrome surface, but their contribution to the final projected image is mostly filtered out by the optical lens.[12]

Aerial images were generated for 180° phase-shift square openings of sizes equal to 1.4λ, 1.8λ and 3λ, and compared to their corresponding thin mask and BL models. Simulations were performed at 248 nm wavelength with a 4X reduction optical system with NA = 0.68, and are displayed in Fig. 3(a)-(c), respectively. They reveal a close agreement between the images generated by both the exact field (solid line) and the BL model (dashed line) in both amplitude and phase plots, markedly reducing the errors caused by the conventional Kirchhoff approximation (dash-dotted line). Usually, the width of the BL controls the variation in peak amplitude, while the imaginary transmission coefficient corrects the phase deviations of the thick mask. These errors differ for different types of mask edge cross-sections, giving different boundary layer parameters to be applied locally in the vicinity of each type of edge profile. Thus each mask edge specification (clear, shifter and shifter with undercut) has its own BL parameters.

3. Simulations

Systematic simulations of rectangular openings with side sizes ranging from 1λ to 6λ, aspect ratios ranging from 3:1 to 1:3, and three different etching profiles for each opening size: 0°, 180° shifter and 180° shifter with 35 nm undercut, provide a means to analyze thick mask effects.[13] The 3D FDTD simulations with coherent,

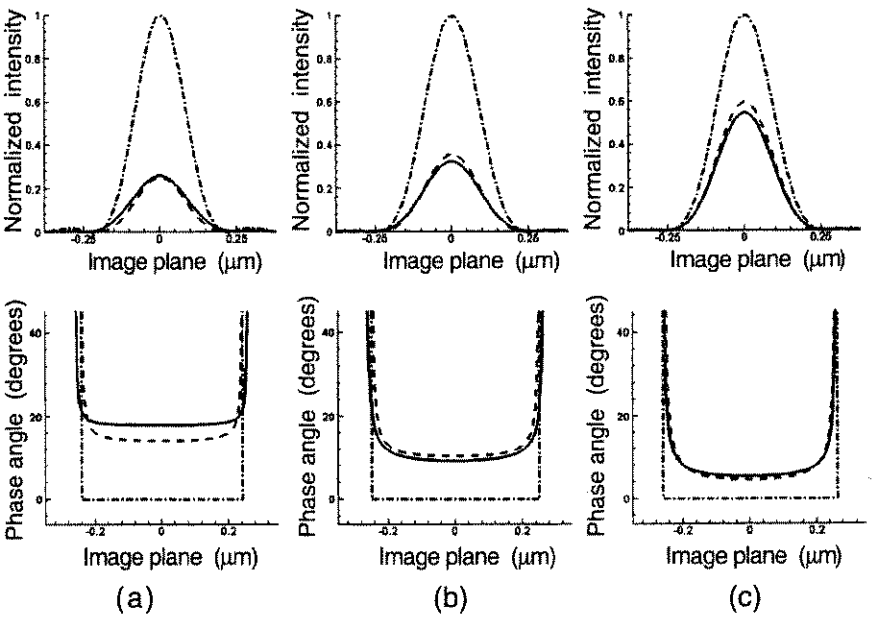

Figure 3. Comparison of both amplitude and phase of aerial images produced by rigorously evaluated EM field solutions on the mask aperture (solid) and both the corresponding Kirchhoff approximation (dash-dotted) and our BL model (dashed), for three sizes of 180°-phase-shift square opening: (a) 1.4λ, (b) 1.8λ and (c) 3λ.

Opening type	Boundary width (nm)		Tangential boundary trans.		Normal boundary trans.	Interior trans.	Minimum opening (nm)	
	I	II	I	II			I	II
Clear	24.8	14.5	$0.0j$	$0.8j$	0	1	248	200
Shifter	55.8	53	$-0.52j$	$-0.3j$	0	−1	300	250
Shifter with 35 nm undercut	37.2	19.3	$-0.9j$	$-0.635j$	0	−1	350	200

Table 1. Width and transmission coefficients of the boundary layer model for different types of openings in typical PSM geometry (cases I and II refer to 248 and 193 nm wavelength imaging systems, respectively).

on-axis illumination provide rigorous results for the EM fields on the masks. Two sets of parameters were evaluated: a 4X projection system with NA = 0.68, operating at λ = 248 nm illumination (case I of Table 1); and a similar 4X system with NA = 0.85, operating at 193 nm (case II in Table 1). The indices of refraction of glass and chrome at 248 nm are 1.5 and (2.5–2j), respectively; whereas at 193 nm they are 1.563 and (0.84–1.65j). Finally, a thicker chrome layer of 95 nm was employed at 193 nm to provide the same absorption of incident light as the 80 nm chrome layer used at 248 nm wavelength.

The relative error in aerial field amplitude produced by the thin mask approximation is measured by the deviations of its real component from the rigorously evaluated field. For the main polarization component, this amplitude deficit at the plane of the wafer follows a reciprocal dependence on the size of the opening for both square and rectangular openings, as observed in Fig. 4(a) for the 248 nm wavelength case, as long as the opening size is measured as the harmonic mean of its width w and its height h. The harmonic mean is defined as twice the product of the sides divided by their sum. As outlined in Eq. (1), this inverse dependence of the relative error amplitude on the opening size indicates that the error can be assumed proportional to a correction width Δd, uniform with the size of the opening and to be applied on all four sides of the thin mask model regardless of polarization:

$$\text{Amplitude deficit} = (\Delta E/E) = (4\Delta d/d) = 2\Delta d(w + h)/wh\ . \qquad (1)$$

The amplitude deficit is, in fact, given by the boundary layer area divided by the total area wh of the opening. Thus the real part of the BL model consists of an opaque layer of zero transmission and fixed width, placed on all four sides of the opening as displayed in Fig. 5(a).

Relative errors of phase produce non-zero values of the imaginary part of the aerial field relative to the thin mask field. Figure 4(b) shows a plot of the imaginary field component *versus* the opening height defined as side length in the direction perpendicular to the electric field polarization, where the same inverse law holds for all square and rectangular openings of all aspect ratios. Any other functional dependence of the phase error, such as the reciprocal of the dimension parallel to polarization, produced a much poorer inverse law fit. Hence, the conclusion that the BL has a purely imaginary transmission coefficient $-j\beta$, that is proportional to the absolute value of the cosine angle between the electric field polarization and the edge direction, arises directly from the dependence in Fig. 4(b) and can be written as follows:

$$\text{Relative imaginary error} = \text{Im}\{\Delta E\}/E = \beta(2\Delta d)/h\ . \qquad (2)$$

The slope of the data in Fig. 4 provides the actual value of this transmission coefficient, needed to compensate for phase deviations of the field and to determine the imaginary part of the BL model as plotted in Fig. 5(b). Final superposition of both real and imaginary parts of the model give the final BL as sketched in Fig. 5(c), with the width and transmission coefficients outlined in Table 1 for the two imaging systems (cases I and II) considered in this chapter.

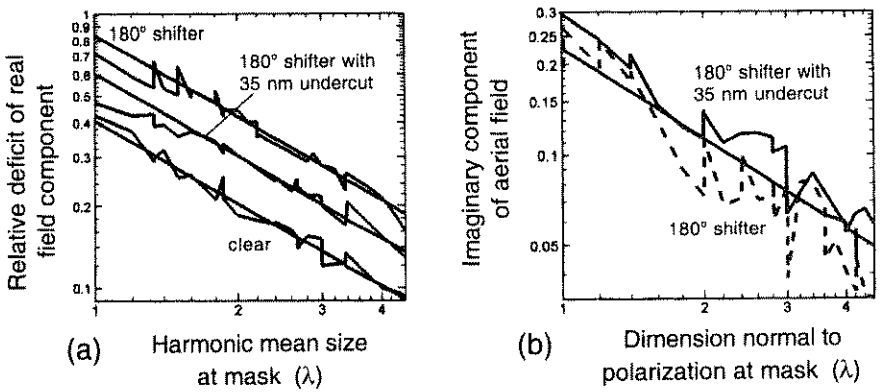

Figure 4. (a) Log-log plot of the relative error in the real component of the aerial electric field *vs.* the harmonic mean of the opening height and width at λ = 248 nm, produced by the thin mask approximation as compared to the rigorously evaluated EM field. (b) Log-log plot of the relative error in the imaginary component as a function of opening height (opening size in the direction perpendicular to polarization).

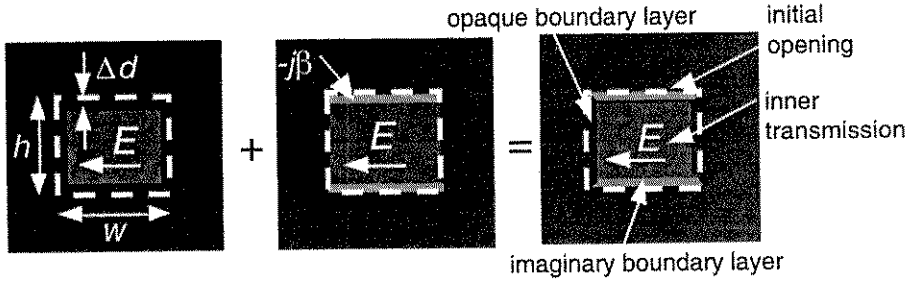

Figure 5. (a) Real component of the BL model. (b) Imaginary component of the BL model. (c) Final BL model as the superposition of both real and imaginary parts.

4. Results

The boundary layer parameters were obtained, for each etching profile, from the slope of the best least-squares straight line fit to the points on Fig. 4, further optimized to minimize the errors but constrained to either zero or a purely imaginary boundary layer transmission. This condition leads to the simplest type of model that still provides satisfactory results. Moreover, even though the boundary layer model was optimized for the field component along the direction of polarization of the incident light, it provided similar error reductions for all cross-field components arising at the exit pupil of a high NA lens. This can be observed for the λ = 193 nm wavelength case in Figs. 6(a)–(c), where the RMS error at the plane of the wafer for both the conventional thin mask model and the

BL model, as compared to the actual image, are displayed for the total electric field as well as individual vector components. Remarkable error reduction occurs even for mask features close to the wavelength. Figure 6(d), on the other hand, plots the phase deviations for 180° phase-shift openings with and without 35 nm undercut, where error reduction by a factor of 7 is achieved for the smallest sizes at 248 nm, where higher phase deviations were observed.

It was further observed that applying the thin mask model to etching profiles of the 180° phase-shifter type without undercut produced the highest RMS errors on the aerial image, as compared to the case with the 35 nm undercut. Even larger errors occurred for mask openings with sides equal to 1λ, which hardly transmit any EM fields and hence were omitted in Fig. 6. Current computational approximations are unable to model such small mask openings, and it is recommended that they should be forbidden in the design rules. The minimum recommended opening is 1.2λ.

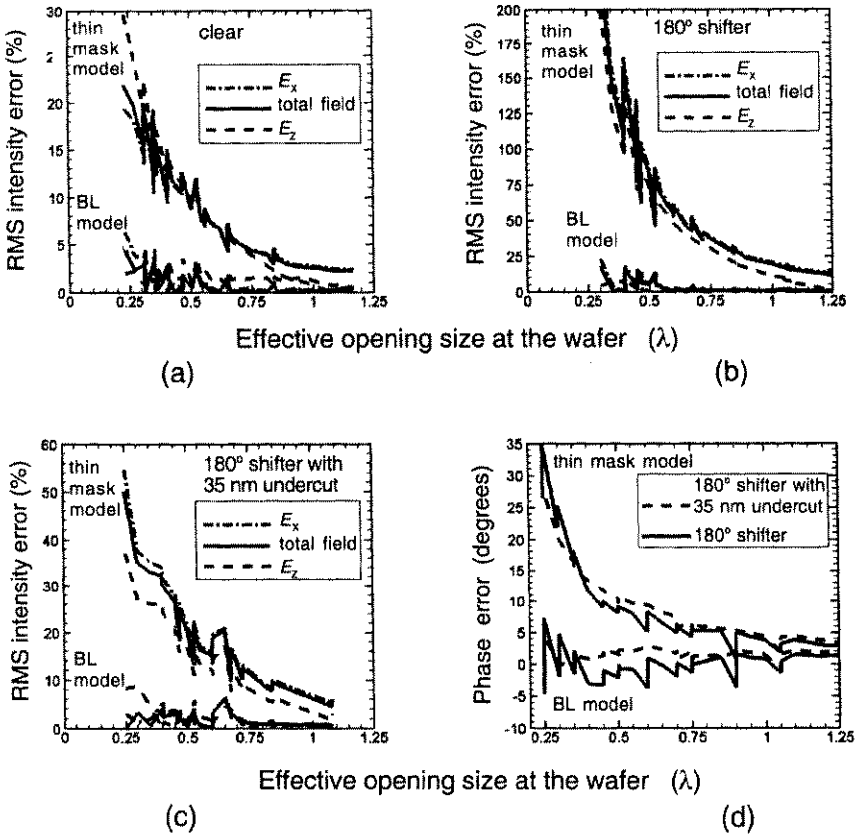

Figure 6. (a)–(c) Root mean squared error on the projected image on the wafer plane of the total electric field and the E_x and E_z components at 193 nm. (d) Field phase in degrees for 180°-phase-shift openings with and without undercut.

Illumination in industrial applications consists of an unpolarized source of partially coherent light that reduces some of the effects associated with coherent illumination. We have simulated partially coherent illumination by assuming Köhler's configuration, where an incoherent light source is located on the focal plane of the condenser lens. The extended source is spatially divided into a number of mutually incoherent point sources. Each of these sources emits a plane wave emerging from the condenser at an angle determined by the source point location with respect to the optical axis. We treat the illumination due to each source point as coherent, polarized plane waves with different angles of incidence. In practice, this requires separate results for both orthogonal (TE and TM) polarizations to be incoherently superposed. The aerial image is then obtained by an incoherent superposition of all the contributions. This procedure, known as Abbe's method, yields the image field amplitude and phase distribution for each illumination angle prior to the source integration, providing the necessary input to our boundary layer model. The equivalent Hopkins method, much used in lithography, provides only intensity and is not as useful for determining boundary layer phase shifts.

Figure 7(a) is a plot of the root mean squared error in the projected image for a partially coherent illumination at 193 nm, NA = 0.85, σ = 0.6 and TE polarization, where σ is the ratio of the condenser lens NA to the NA of the projection optics. The same boundary layer parameters of Table 1 were applied to approximate the near field effects of 180°-phase-shift openings, even though Table 1 applied only to the on-axis illumination case. Figure 7(b) displays the effect of the de-focusing (depth-of-field) errors on intensity. The effect of defocusing is small. Phase errors are expected to be more critically affected by defocusing.

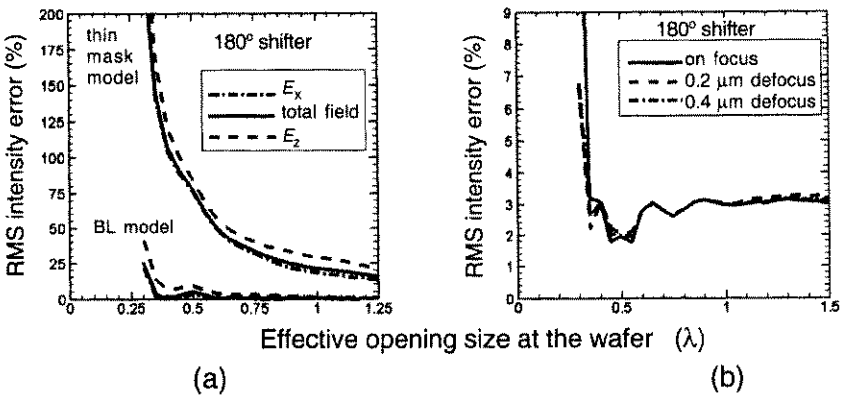

Figure 7. (a) Root mean squared error in the projected image for partially coherent illumination at 193 nm, NA = 0.85, σ = 0.6 and TE polarization, generated by the approximated models of 180°-phase-shift openings, as compared with the rigorously evaluated field due to the same illumination. (b) The effect of depth of field error on the intensity.

5. Conclusions

Although thick mask effects decay slowly with the size of the opening, the key result of our simulations is that this decay can be interpreted, to a good approximation, as a locally determined, fixed-size edge effect, with just two parameters: width and transmission coefficient of the boundary layer. We observed how the relative errors of the real and imaginary field components on the wafer follow an inverse law on the opening mean size and height, respectively. This allowed us to model them as a simple boundary layer of fixed width and transmission coefficient. This new boundary layer model incorporates thick mask effects and polarization dependencies, that greatly improves the accuracy of aerial image computation in photolithography simulations at a reasonable computational cost.

Appendix A: Vector formulation of the imaging process

Scalar diffraction theory[11] yields accurate results of the field in the image space when numerical apertures up to 0.7 are employed,[14] but it fails to account for the polarization and oblique direction of propagation of the vector components of the EM field with higher *NA*. Rigorous vector diffraction theory was first applied to optical imaging and exposure process for optical lithography by Yeung[5] and subsequently analyzed by several other authors in more recent articles.[4,6]

In the determination of the vector representation of EM fields in the image space, Wolf's[15] generalization of Debye's integral formulation can be applied. Based on the notation of Fig. A1, the expression takes the form:

$$\boldsymbol{E}_{\mathrm{IMAGE}}(x', y', z') = (j/\lambda) \iint_{s_X^2 + s_Y^2 \le 1} \frac{\boldsymbol{a}(s_X, s_Y)}{s_Z} e^{-jk[\Phi(s_X, s_Y) + \hat{\mathbf{s}}\cdot\mathbf{r}']} \, ds_X \, ds_Y \qquad (A.1)$$

This formulation is based on geometrical optics and provides the optical image in the neighborhood of the lens focal plane in terms of a superposition of plane waves propagating with all direction cosines (s_X, s_Y) that fill the exit pupil aperture.[11] The phase term $\Phi(s_X, s_Y)$ denotes the aberration function with respect to an ideal spherical wavefront converging towards the focal point (a constant phase term has been dropped for simplicity). In deriving of Eq. (A.1), Kirchhoff boundary conditions were applied on the exit pupil aperture. Therefore, it is accurate at distances from the pupil plane that satisfy the condition[16] $NA >> (\lambda/f)^{1/2}$ (equivalent to the condition that the Fresnel number is much larger than unity), where f represents the geometrical focal distance. With focusing distances of the order of a few mm,[14] and numerical apertures as high as 0.85 for 193 nm wavelength lithography, this condition guaranties that the Debye integral representation yields essentially the same results for the fields in the focal region as techniques based on Huygens-Fresnel principle[16] or plane-wave decompositions.[4]

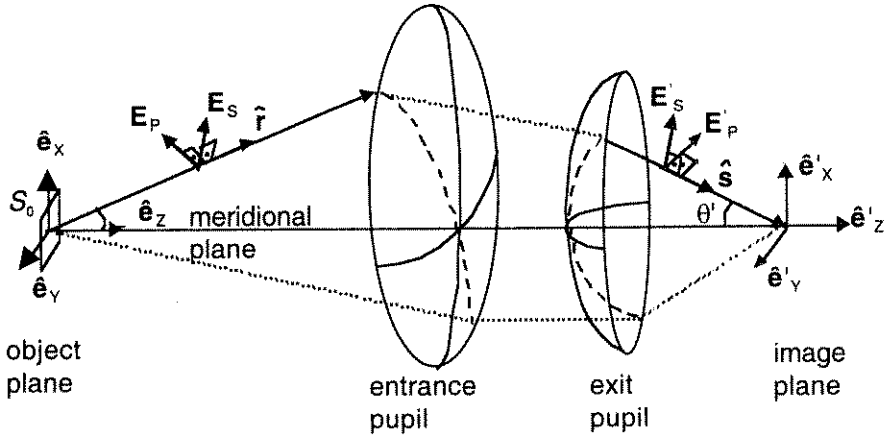

Figure A.1. Schematic optical projection system setup. Object space coordinates are denoted (x, y, z), while image space coordinates are denoted (x', y', z'). Each propagation direction $\hat{\mathbf{r}}$ of waves diffracted by the object forms the meridional plane together with the optical axis $\hat{\mathbf{e}}_Z$. The corresponding wave direction $\hat{\mathbf{s}}$ of the wave converging towards the image plane from the exit pupil lies on the same meridional plane. Field components along the normal and parallel directions to this plane, $\mathbf{E}_S$ and $\mathbf{E}_P$, maintain the same amplitude, denoted $\mathbf{E}'_S$ and $\mathbf{E}'_P$ in the image space, as the wave vector $k_0\hat{\mathbf{r}}$ rotates onto $k_0\hat{\mathbf{s}}$.

Rigorous electromagnetic theory was also utilized to derive the fields at the entrance pupil by means of the well-known Franz formula[17] for the diffraction of fields, which reduces to equation (A.2) as the observation point on the entrance pupil recedes to the far-field zone:[18,19]

$$\boldsymbol{E}_{\mathrm{ENTRANCE}}(r_X, r_Y) =$$

$$= (e^{-jk_0 r}/j2\lambda r)\, \mathcal{F}\{[\eta(\hat{\mathbf{e}}_Z \mathrm{x} \boldsymbol{H}_0) - \eta[(\hat{\mathbf{e}}_Z \mathrm{x} \boldsymbol{H}_0)\cdot\hat{\mathbf{r}}]\hat{\mathbf{r}} - (\hat{\mathbf{e}}_Z \mathrm{x} \boldsymbol{E}_0)\mathrm{x}\hat{\mathbf{r}}]; r_X/\lambda, r_Y/\lambda\} \qquad (A.2)$$

where $\mathcal{F}$ denotes the Fourier transform evaluated at spatial frequencies r_X/λ and r_Y/λ, whereas $\boldsymbol{E}_0$ and $\boldsymbol{H}_0$ are the electric and magnetic fields on the exit surface of the photomask. In our calculations, these fields on the mask are either rigorous 3D electromagnetic solutions, or stepwise discontinuous fields resulting from the direct application of Kirchhoff boundary conditions on the mask surface.

Only image points of small linear dimensions around the optical axis $\hat{\mathbf{e}}_Z$, as compared to the distance r, are of interest in this analysis, meaning that, according to the method of stationary phase,[11] only points about the optical axis will contribute significantly to the diffraction integral. Therefore the unit vector $\hat{\mathbf{r}}$ pointing toward the observation point $\mathbf{r}$ on the entrance pupil reduces to Eq. (A.3a). It follows from Eq. (A.2) that for any $\hat{\mathbf{r}}$ the fields on the entrance pupil behave locally as plane waves and are transverse to the direction of propagation:

$$\hat{\mathbf{r}} = \mathbf{r}/r = r_X\hat{\mathbf{e}}_X + r_Y\hat{\mathbf{e}}_Y + r_Z\hat{\mathbf{e}}_Z = \sin\theta\cos\varphi\,\hat{\mathbf{e}}_X + \sin\theta\sin\varphi\,\hat{\mathbf{e}}_Y + \cos\theta\,\hat{\mathbf{e}}_Z \qquad (A.3a)$$

$$\hat{\mathbf{s}} = \mathbf{s}/s = s_X\hat{\mathbf{e}}_X + s_Y\hat{\mathbf{e}}_Y + s_Z\hat{\mathbf{e}}_Z = -\sin\theta'\cos\varphi\,\hat{\mathbf{e}}_X - \sin\theta'\sin\varphi\,\hat{\mathbf{e}}_Y + \cos\theta'\,\hat{\mathbf{e}}_Z \qquad (A.3b)$$

Turning our attention to Eq. (A.1) of the aerial image, the amplitude function $a(s_X,s_Y)$ can be related to the field at each point of the entrance pupil, given by Eq. (A.2), by tracing the geometrical ray propagation and polarization state through the optical system. A detailed knowledge of the optical design is therefore needed. High resolution image formation, on the other hand, relies on nearly diffraction-limited imaging characteristics of refractive lenses at the illumination wavelength,[14] which imposes tight design specifications on lens manufactures and allows us to assume lossless, isoplanatic (phase-invariant) imaging lenses. Under these circumstances, each ray traces a path that lies on its meridional plane (plane formed by the ray direction $\hat{\mathbf{r}}$ and the optical axis $\hat{\mathbf{e}}_Z$) and, although the ray direction $\hat{\mathbf{r}}$ will be rotated onto $\hat{\mathbf{s}}$ as it propagates through the lens (according to Eqs. (A.3a) and (A.3b)), the polarization vector will, according to Fresnel refraction formula, maintain an approximately constant angle with this plane if the angles of incidence at the various surfaces in the system are small.[5,20] Thus, the field amplitudes along the normal and parallel directions to the plane will remain unchanged by refraction during propagation through the optical system, except a for geometrical factor arising from the conservation of energy:

$$|E_{\text{EXIT}}(s_X,s_Y)|^2\, da' = |E_{\text{ENTRANCE}}(r_X,r_Y)|^2\, da\,. \qquad \text{(A.4)}$$

Moreover, the angle θ between the incident ray and the entrance pupil, and the angle θ' between the outgoing ray and the exit pupil, must satisfy the sine condition $\sin\theta = M\sin\theta'$ where M denotes the demagnification of the lens (usually 1/4 or 1/5). The spatial frequencies in the image space are therefore related to those in the object space according to $s_X = -r_X/M$ and $s_Y = -r_Y/M$ and the final relationship between the field amplitude at the exit and entrance pupils is as follows:

$$a(s_X, s_Y) =$$

$$(M\alpha/2\lambda)\, \mathcal{T}\cdot\mathcal{F}\left\{\left[\eta(\hat{\mathbf{e}}_Z \mathrm{x} \boldsymbol{H}_0) - \eta[(\hat{\mathbf{e}}_Z \mathrm{x} \boldsymbol{H}_0)\cdot\hat{\mathbf{r}}]\hat{\mathbf{r}} - (\hat{\mathbf{e}}_Z \mathrm{x} \boldsymbol{E}_0)\mathrm{x}\hat{\mathbf{r}}\right];\, r_X/\lambda,\, r_Y/\lambda\right\} \qquad \text{(A.5)}$$

where $\alpha \equiv (\cos\theta'/\cos\theta)^{1/2}$, for each of the rays at the exit pupil with direction cosines (s_X, s_Y, s_Z). Polarization rotation is represented by the tensor $\mathcal{T}$, obtained by means of the meridional plane approximation and provided in Appendix B.

Simulations have been performed for polarized illumination along the **x**-axis and a 4X reduction ratio, such that even with high NA = 0.7–0.9 of the imaging lens, the angle described by the collected waves on the entrance pupil is small. Under these circumstances, cross-polarized components of the field on the mask are several orders of magnitude smaller and can be neglected, while the main polarization components satisfy, with an accuracy of 92% based on rigorous electromagnetic simulations,[2] the following condition within the lens NA:

$$\mathcal{F}\{\boldsymbol{H}_0(\mathbf{r})\}\cdot\hat{\mathbf{e}}_Y = (\varepsilon_0/\mu_0)^{1/2}\,[\hat{\mathbf{r}} \times \mathcal{F}\{\boldsymbol{E}_0(\mathbf{r})\}]\cdot\hat{\mathbf{e}}_Y \qquad \text{(A.6)}$$

This condition significantly simplifies Eq. (A.5) and was first applied to all field components by Yeung in his extension of Hopkins theory,[21] which may not be accurate for cross-polarized components. Nevertheless, when applied to the main polarization component, Eq. (A.6) yields a simple expression for the electric field on the entrance pupil:

$$\boldsymbol{E}_{\text{ENTRANCE}} = \hat{\mathbf{e}}_Y\,(je^{-jk_0r}/\lambda r)\,\mathcal{F}\{\boldsymbol{E}_{0Y};\, r_X/\lambda,\, r_Y/\lambda\}\cos\theta \qquad \text{(A.7)}$$

which can now be treated as a scalar quantity consistent with the scalar Huygens-Fresnel formulation.[4,11]

Finally, while irradiance of the aerial image is evaluated as the magnitude of the time-averaged Poynting vector, the absorbed energy within the photoresist and, therefore, the final image distribution is proportional to the squared electric field of the light propagating through it since it is a non-magnetic material.[4] Therefore only the electric field of the aerial image needs to be evaluated.

Appendix B: polarization tensor

For each ray direction (s_X, s_Y, s_Z), polarization rotation can be expressed via a tensor $\mathcal{T}$ obtained by decomposing the fields into their projections along the directions normal and parallel to the meridional plane, and by applying the condition that the polarization angle with respect to this plane should remain approximately constant through the projection system. The resultant tensor components are:

$$\mathcal{T} = \begin{vmatrix} \mathcal{T}_{XX} & \mathcal{T}_{XY} & -\mathcal{T}_{XZ} \\ \mathcal{T}_{XY} & \mathcal{T}_{YY} & -\mathcal{T}_{YZ} \\ \mathcal{T}_{XZ} & \mathcal{T}_{YZ} & \mathcal{T}_{ZZ} \end{vmatrix} \qquad \text{(B.1)}$$

where

$$T_{XX} = \frac{s_Y^2 + s_X^2(s_Zr_Z - M(s_X^2 + s_Y^2))}{(s_X^2 + s_Y^2)}, \qquad T_{YY} = \frac{s_X^2 + s_Y^2(s_Zr_Z - M(s_X^2 + s_Y^2))}{(s_X^2 + s_Y^2)},$$

$$T_{XY} = \frac{-s_Xs_Y(1 - s_Zr_Z + M(s_X^2 + s_Y^2))}{(s_X^2 + s_Y^2)}, \qquad T_{ZZ} = s_Zr_Z - M(s_X^2 + s_Y^2),$$

$$T_{XZ} = -s_X(r_Z + Ms_Z), \qquad \text{and} \qquad T_{YZ} = -s_Y(r_Z + Ms_Z).$$

These results are consistent with the so-called "polarization state matrix" based on the trigonometrically determined polarization transformation by Mansuripur,[22] as long as the scalar approximation is applied in the object space, that is, $s_X, s_Y \ll r_Z \sim 1$.

Acknowledgments

This work was supported by grant number DAAD19-99-1-0196 from U.S. Department of the Army, and by the "La Caixa" Foundation Scholarship Program (Spain).

References

1. M. S. Yeung and E. Barouch, "Limitation of the Kirchhoff boundary conditions for aerial image simulation in 157 nm optical lithography," *IEEE Electron Dev. Lett.* **21**, 433 (2000).
2. A. K. Wong and A. R. Neureuther. "Rigorous three-dimensional time-domain finite-difference electromagnetic simulation for photolithographic applications," *IEEE Trans. Semicond. Manufacturing* **8**, 419 (1995).
3. A. K Wong and A. R Neureuther. "Mask topography effects in projection printing of phase-shifting masks," *IEEE Trans. Electron Dev.* **41**, 895 (1994).
4. D. G. Flagello, T. Milster, and A. E. Rosenbluth, "Theory of high-NA imaging in homogeneous thin films" *J. Opt. Soc. Am. A* **13**, 53 (1996).
5. M. S. Yeung, "Modeling high numerical aperture optical lithography" *Proc. SPIE* **922**, 149 (1988).
6. K. Adam, Y. Granik, A. Torres, and N. Cobb, "Improved modeling performance with an adapted vectoral formulation of the Hopkins imaging equation" *Proc. SPIE* **5040**, 78 (2003).
7. Y. Borodovsky *et. al.*, "Lithography strategy for 65 nm node," *Proc. SPIE* **4754**, 1 (2002).
8. Konstantinos Adam and Andrew R. Neureuther. "Simplified models for edge transitions in rigorous mask modeling," *Proc. SPIE* **4346**, 331 (2001).
9. Pei-Yang Yan, "Understanding Bossung curve asymmetry and focus shift effect in EUV lithography," *Proc. SPIE* **4562**, 1 (2001).
10. M. Lam, K. Adam, and A. Neureuther, "Domain decomposition methods for simulation of printing and inspection of phase defects," *Proc. SPIE* **5040**, 1492 (2003).
11. M. Born and E. Wolf, *Principles of Optics*, 6th ed., London: Pergamon Press, 1987.
12. G. Wojcik, J. Mould, R. Ferguson, R. Martino, and K. K. Low. "Some image modeling issues for i-line, 5X phase shifting masks," *Proc. SPIE*, **2197**, 455 (1994).
13. J. Tirapu-Azpiroz, P. Burchard, and E. Yablonovitch, "Boundary layer model to account for thick mask effects in photolithography," *Proc. SPIE* **5040**, 1611 (2003).
14. H. J. Levinson, *Principles of Lithography*, Bellingham, WA: SPIE Press, 2001.
15. E. Wolf, "Electromagnetic diffraction in optical systems. I. An integral representation of the image field," *Proc. Roy. Soc. A* **253**, 349 (1959).
16. E. Wolf and Y. Li, "Conditions for the validity of the Debye integral representation of focused fields," *Optics Commun.* **39**, 205 (1981).
17. See C. T. Tai. "Direct integration of field equations," chapter in: J. A. Kong, ed., *Progress in Electromagnetic Research*, Vol. 28, Boston: EMW Publishing, 2000, pp. 339–359.
18. S. Silver, *Microwave Antenna Theory and Design*, New York: McGraw-Hill, 1949.

19. R. Mittra, *Computer Techniques for Electromagnetics*, Washington: Hemisphere Publishing Co., 1987.
20. B. Richards and E. Wolf, "Electromagnetic diffraction in optical systems. II. Structure of the image in an aplanatic system," *Proc. Roy. Soc. A* **253**, 358 (1959).
21. M. S. Yeung, D. Lee, R. Lee, and A. R. Neureuther, "Extension of the Hopkins theory of partially coherent imaging to include thin-film interference effects," *Proc. SPIE* **1927**, 452 (1993).
22. M. Mansuripur, "Distribution of light at and near the focus of high-numerical aperture objectives," *J. Opt. Soc. Am. A* **3**, 2086 (1986).